OBSERVATIONS ON MOHR-COULOMB PLASTICITY UNDER PLANE-STRAIN

W.M. Coombs[1], R.S. Crouch[2] and C.E. Heaney[3]

ABSTRACT

Linear elastic-perfect plasticity using the Mohr-Coulomb yield surface is one of the most widely used pressure-sensitive constitutive models in engineering practice. In the area of geotechnical engineering a number of problems, such as cavity expansion, embankment stability and footing bearing capacity, can be examined using this model together with the simplifying assumption of plane-strain. This paper clarifies the situation regarding the direction of the intermediate principal stress in such an analysis and reveals a unique relationship between hydrostatic pressure and the principal stress ratio for Mohr-Coulomb and Tresca perfect plasticity under those plane-strain conditions. The rational relationship and direction of the intermediate principal stress are illustrated through both material point and finite-element simulations. The latter involves the analysis of a rigid strip footing bearing onto a weightless soil and the finite deformation expansion of a cylindrical cavity.

Keywords: Intermediate principal stress, Mohr-Coulomb, Tresca, elasto-plasticity, plane-strain analysis, geomaterials.

INTRODUCTION

The compressive strength and inelastic deformation of particulate materials, such as soils, fractured rocks, grains and powders, are dependent on the effective hydrostatic pressure. This behaviour is characteristic of media where the mechanics is dominated by frictional forces. The linear elastic-perfectly plastic Mohr-Coulomb (referred to hereafter as M-C) model is one of the most widely used

[1]Lecturer, Durham University, School of Engineering & Computing Sciences, Science Site, South Road, Durham, DH1 3LE, United Kingdom. E-mail: w.m.coombs@durham.ac.uk.
[2]Professor, Durham University, School of Engineering & Computing Sciences, Science Site, South Road, Durham, DH1 3LE, United Kingdom.
[3]Marie Curie Research Fellow, Plaxis BV, Delftechpark 53, 2628 XJ Delft, The Netherlands.

pressure-sensitive constitutive models which can capture this behaviour in an idealised way. The original M-C criterion was first expressed in three dimensions by Shield (1955), although Prager and Bishop had also established this in unpublished work. With zero friction, the M-C model reduces to the pressure-invariant Tresca formulation as a special case. That model has been extensively used when analysing the elasto-plastic behaviour of metals (see, for example, Ewing and Griffiths (1971); Griffiths and Owen (1971)).

A number of common geotechnical problems, such as footing displacement, embankment stability and cavity expansion, lend themselves to two-dimensional plane-strain analysis. Such analyses can provide a useful approximation of the structural behaviour whilst requiring only modest computational expenditure (when compared to three-dimensional analyses).

This paper presents the *rational relationship* between the relative magnitude of the intermediate principal stress (b, defined below) and the hydrostatic pressure (ξ) for the M-C and Tresca constitutive models under plane-strain conditions. This relationship expresses the principal stress locus that elasto-plastic states are required to follow over the M-C yield surface.

Isotropic constitutive formulations (such as the M-C and Tresca models) allow the relations to be described using principal stress and strain quantities, providing a clear geometric interpretation of the material state. All of the findings of this paper are presented using principal stresses and strains, with a tension positive notation. The principal stress ratio is defined here as

$$b = \frac{\sigma_1 - \sigma_2}{\sigma_1 - \sigma_3} \qquad \in [0, 1], \tag{1}$$

where σ_1 and σ_3 are the major (most tensile) and minor (most compressive) principal stresses respectively, such that $\sigma_1 \geq \sigma_2 \geq \sigma_3$. The hydrostatic stress is defined as $\xi = \mathrm{tr}\big([\sigma]\big)/\sqrt{3} = (\sigma_1 + \sigma_2 + \sigma_3)/\sqrt{3}$, where $\mathrm{tr}\big([\cdot]\big)$ denotes the trace of $[\cdot]$. ξ is not the mean stress; it corresponds to the distance along the hydrostatic axis from the origin in Haigh-Westergaard stress space. The principal stress ratio is related to the Lode angle, θ, through

$$b = \frac{1 + \sqrt{3}\tan(\theta)}{2}, \qquad \text{where} \qquad \theta = \frac{1}{3}\arcsin\left(\frac{-3\sqrt{3}}{2}\frac{J_3}{J_2^{3/2}}\right) \quad \in \big[-\pi/6, \pi/6\big]. \tag{2}$$

The deviatoric stress invariants are given by $J_2 = \text{tr}([s]^2)/2$ and $J_3 = \text{tr}([s]^3)/3$, where the *traceless* deviatoric stress matrix $[s] = [\sigma] - \xi[I]/\sqrt{3}$ and $[I]$ is the third-order identity matrix.

The layout of the paper is as follows. Initially the M-C constitutive relations are presented, including the isotropic linear stress-elastic strain law, yield criterion and plastic flow direction. The next section restricts the M-C constitutive model to the case of plane-strain analysis and derives the relationship between the hydrostatic stress, ξ, and the principal stress ratio, b. The limiting cases of triaxial compression ($b = 0$; $\sigma_2 = \sigma_1$) and extension ($b = 1$; $\sigma_2 = \sigma_3$) are also considered. The simplification of the M-C ξ versus b relationship for the Tresca constitutive model is given and the rational relationship extended to account for inelastic straining in the out-of-plane direction induced by the corners present in the yield envelopes. Following this, a simple material point investigation is used to investigate the assumption that the out-of-plane stress is indeed the intermediate principal stress. Three finite-element investigations using the M-C model are then presented: (i) a simple two-element simulation, (ii) an analysis of a rigid strip footing bearing onto a weightless soil and (iii) a finite deformation cavity expansion simulation. These simulations provide numerical verification of the ξ-b relationship for the M-C model. Conclusions are drawn in the final section.

MOHR-COULOMB CONSTITUTIVE FORMULATION

The constitutive laws for (and the algorithmic treatment of) the isotropic linear elastic-perfectly plastic M-C model are widely available in literature (for example, see the papers by Clausen et al. (2006, 2007) and references cited therein). Here, to aid clarity, the basic equations required in the later sections of this paper are reviewed briefly.

Linear isotropic elasticity

The following isotropic linear elastic stiffness matrix

$$\left[D^{\mathrm{e}}\right] = \frac{E}{(1+\nu)(1-2\nu)}\Big[(1-2\nu)[I] + \nu[1]\Big], \tag{3}$$

provides the relationship between the vectors containing the principal Cauchy stresses, $\{\sigma\}$, and the principal elastic strains, $\{\varepsilon^{\mathrm{e}}\}$

$$\{\sigma\} = \left[D^{\mathrm{e}}\right]\{\varepsilon^{\mathrm{e}}\}. \tag{4}$$

3

In (3), E is Young's modulus, ν Poisson's ratio and [1] is the third-order matrix populated with ones. The total strain vector is split into elastic (recoverable) and inelastic (irrecoverable) components as follows; $\{\varepsilon\} = \{\varepsilon^{\mathrm{e}}\} + \{\varepsilon^{\mathrm{p}}\}$.

Inelasticity

The M-C criterion assumes that plastic frictional sliding will occur once the minor principal stress, σ_3, falls below some proportion of the major principal stress, σ_1. This can be defined using the following yield function

$$f = k\sigma_1 - \sigma_3 - \sigma_c = 0, \qquad \text{where} \qquad k = \frac{1 + \sin(\phi)}{1 - \sin(\phi)} \qquad \text{and} \qquad \sigma_c = 2c\sqrt{k}. \qquad (5)$$

ϕ is the internal friction angle, c the *cohesion* and σ_c defines the uniaxial compressive yield strength. The M-C yield surface is shown in Figure 1 using (i) a deviatoric section viewed down the hydrostatic axis and (ii) an isometric view of principal stress space.

The non-associated plastic flow direction is given by

$$\{g_{,\sigma}\} = \{k_g \quad 0 \quad -1\}^T, \qquad \text{where} \qquad k_g = \frac{1 + \sin(\phi_g)}{1 - \sin(\phi_g)} \qquad (6)$$

and $\phi_g \in [0, \phi]$ is the plastic dilation angle, such that the rate of inelastic straining is given by

$$\{\dot{\varepsilon}^{\mathrm{p}}\} = \dot{\gamma}\{g_{,\sigma}\}. \qquad (7)$$

$\dot{\gamma}$ is the plastic consistency parameter. This multiplier is subject to the Kuhn-Tucker-Karush conditions: $\dot{\gamma} \geq 0$, $f \leq 0$ and $\dot{\gamma}f = 0$ (that is, a stress state can only lie on, or within, the perfectly plastic yield envelope).

THE HYDROSTATIC STRESS VERSUS PRINCIPAL STRESS RATIO RELATIONSHIP

In all that follows it is assumed that once the material point has reached yield the intermediate principal stress is in the out-of-plane direction. The validity of this assumption is examined later in the paper. Combining this assumption with the direction of plastic flow from (6), we obtain the

4

following relation between the principal values of stress and elastic strain

$$\{\sigma\} = \left[D^{\mathrm{e}}\right]\{\varepsilon_1^{\mathrm{e}} \quad 0 \quad \varepsilon_3^{\mathrm{e}}\}^T.$$ (8)

Inverting the elastic stiffness matrix and using the plane-strain condition in (8), we arrive at the following relationship between the principal stresses

$$\sigma_2 = \nu(\sigma_1 + \sigma_3).$$ (9)

Using ξ, we can express the intermediate principal stress as

$$\sigma_2 = \frac{\sqrt{3}\xi\nu}{(1+\nu)}.$$ (10)

Given (5), the minor principal stress may now be written as

$$\sigma_3 = k\sigma_1 - \sigma_c.$$ (11)

From (10), (11) and ξ, we obtain the major principal stress as

$$\sigma_1 = \frac{\sigma_c + \sqrt{3}\xi/(1+\nu)}{(1+k)}.$$ (12)

Equations (10) to (12) show that the values of σ_1, σ_2 and σ_3 are each determined by ξ. The locus traced by this equations is shown on the M-C yield surface in principal stress space for $\phi = \pi/9$, $\nu = 0.2$ and $c = 100\mathrm{kPa}$ in Figure 1 (ii). Substituting (10) to (12) into (1), the principal stress ratio becomes

$$b = \frac{\sqrt{3}\xi(1 - \nu(1+k)) + \sigma_c(1+\nu)}{(1-k)\sqrt{3}\xi + 2\sigma_c(1+\nu)},$$ (13)

or alternatively

$$\xi = \frac{\sigma_c(1+\nu)(1-2b)}{\sqrt{3}\big(b(1-k) + \nu(1+k) - 1\big)}.$$ (14)

5

¹⁰⁰ (14) provides an injective function between b and ξ.

Compression and extension meridians

¹⁰² From (14) we see that b attains a value of zero at the following hydrostatic stress

$$\xi_{b=0} = \frac{\sigma_c(1+\nu)}{\sqrt{3}(\nu(1+k)-1)}; \qquad (15)$$

¹⁰³ point C in Figure 1 (ii). For hydrostatic stresses less than this value, (13) and (14) are no longer
¹⁰⁴ valid as the stress point is situated on the compression meridian ($\sigma_1 = \sigma_2 > \sigma_3$). For Poisson's
¹⁰⁵ ratio $\nu \geq 1/(1+k)$, the stress state will never reach the compression meridian and instead a limit
¹⁰⁶ is imposed on the minimum attainable principal stress ratio, given by

$$\lim_{\xi \to -\infty} b = \frac{1 - \nu(1+k)}{1-k} \qquad \nu \in [1/(1+k), 0.5]. \qquad (16)$$

¹⁰⁷ The hydrostatic stress associated with $b = 1$ is given by

$$\xi_{b=1} = \frac{\sigma_c(1+\nu)}{\sqrt{3}(k - \nu(1+k))}; \qquad (17)$$

¹⁰⁸ point B in Figure 1 (ii). The stress will be located on the extension meridian ($\sigma_3 = \sigma_2 < \sigma_1$)
¹⁰⁹ for hydrostatic pressures $\xi_{b=1} \leq \xi \leq \xi_c$, where $\xi_c = \sqrt{3}c\cot(\phi)$ identifies where the yield surface
¹¹⁰ intersects the hydrostatic axis (point A in Figure 1 (ii)).

¹¹¹ In order to investigate the limits further, the M-C constitutive model was subjected to one
¹¹² dimensional straining until reaching yield. A Young's modulus of $E = 10\text{GPa}$ and a Poisson's ratio
¹¹³ of $\nu = 0.3$ were used for the material's elastic properties. In this simple illustration, the M-C model
¹¹⁴ had a friction angle of $\phi = \pi/9$ (20 degrees) and an apparent cohesion of $c = 100\text{kPa}$. Under
¹¹⁵ compression the constitutive model reached yield at the following normalised stress state

$$\frac{\{\sigma\}}{c} = \{-9.724 \qquad -9.724 \qquad -22.690\}^T,$$

¹¹⁶ with a normalised hydrostatic pressure of $(\xi/c) = -24.33$. This state agrees with the compressive

theoretical limit provided by (15). Under extension, the stress path reaches yield at a normalised hydrostatic pressure of $(\xi/c) = 1.90$, again agreeing with the theoretical limit when $b = 1$ given by (17). Therefore, the limits provided by (15), for $b = 0$ on the compression meridian, and (17), when $b = 1$ on the extension meridian, define the intersection of the stress path with the M-C yield surface for this uniaxial strain case.

The special case of Tresca (frictionless) yielding with associated flow

In the limiting case where $\phi = 0$ (that is, Tresca plasticity), the yield criterion (5) and the direction of associated plastic flow (6) become

$$f = \sigma_1 - \sigma_3 - 2c = 0 \qquad \text{and} \qquad \{g_{,\sigma}\} = \{1 \quad 0 \quad -1\}^T \tag{18}$$

as $k(\phi = 0) = 1$. Following the same steps as for the case of M-C, we obtain the principal stresses as

$$\sigma_1 = \frac{\sqrt{3}\xi}{2(1+\nu)} + c \qquad \sigma_2 = \frac{\sqrt{3}\xi\nu}{(1+\nu)} \qquad \text{and} \qquad \sigma_3 = \sigma_1 - 2c. \tag{19}$$

The principal stress ratio then becomes

$$b = \frac{\sqrt{3}(1-2\nu)}{4c(1+\nu)}\xi + \frac{1}{2} = a_v\xi + \frac{1}{2} \qquad \text{or} \qquad \xi = \frac{b - 1/2}{a_v}, \tag{20}$$

where the definition of a_v is self evident. Thus for plane-strain analysis using the Tresca yield criterion, a linear relationship exists between ξ and b. Similar to the M-C relationship, the limits on (20) are obtained as

$$\xi_{b=0} = \frac{2c(1+\nu)}{\sqrt{3}(2\nu - 1)} \qquad \text{and} \qquad \xi_{b=1} = \frac{2c(1+\nu)}{\sqrt{3}(1 - 2\nu)} \qquad \text{with} \qquad \xi_{b=0} = -\xi_{b=1}. \tag{21}$$

Beyond these limits, the stress state will be located on the compression ($\xi \leq \xi_{b=0}$) or extension meridian ($\xi \geq \xi_{b=1}$).

Yield condition at the corners

When material states are on the compression or extension meridians, the direction of plastic flow is no longer uniquely defined. However, given a total strain increment, the plastic strain increment (and therefore the elastic strain and stress increments) can be obtained using the method proposed by Koiter (1953). The non-uniqueness of the plastic strain direction can lead to inelastic deformation in the out-of-plane direction.

For the case when $\varepsilon_2^{\mathrm{e}} \neq 0$, the principal Cauchy stresses are given by

$$\{\sigma\} = \left[D^{\mathrm{e}}\right] \{\varepsilon_1^{\mathrm{e}} \quad \varepsilon_2^{\mathrm{e}} \quad \varepsilon_3^{\mathrm{e}}\}^T \tag{22}$$

Subtracting the intermediate elastic strain from each component of the principal strain vector and adding the equivalent hydrostatic pressure, σ^e, to the right hand side to (22), gives rise to the following relationship

$$\{\sigma\} = \left[D^{\mathrm{e}}\right] \{(\varepsilon_1^{\mathrm{e}} - \varepsilon_2^{\mathrm{e}}) \quad 0 \quad (\varepsilon_3^{\mathrm{e}} - \varepsilon_2^{\mathrm{e}})\}^T + \sigma^{\mathrm{e}}\{1\}, \tag{23}$$

where $\sigma^{\mathrm{e}} = \varepsilon_2^{\mathrm{e}} E/(1 - 2\nu)$ and $\{1\}$ indicates a 3 component vector populated with ones. Following the same procedure as when deriving (13), we can express the principal stresses as

$$\sigma_1 = \frac{\sqrt{3}\xi - (1 - 2\nu)\sigma^{\mathrm{e}} + (1 + \nu)\sigma_c}{(1 + k)(1 + \nu)}, \qquad \sigma_2 = \frac{\sqrt{3}\xi\nu + (1 - 2\nu)\sigma^{\mathrm{e}}}{(1 + \nu)} \qquad \text{and} \qquad \sigma_3 = k\sigma_1 - \sigma_c. \tag{24}$$

Substituting (24) into (1), we obtain the following relationship for the principal stress ratio

$$b = \frac{\sqrt{3}\xi\big(1 - \nu(1 + k)\big) - (1 - 2\nu)(2 + k)\sigma^{\mathrm{e}} + \sigma_c(1 + \nu)}{\big(\sqrt{3}\xi - (1 - 2\nu)\sigma^{\mathrm{e}}\big)(1 - k) + 2\sigma_c(1 + \nu)}. \tag{25}$$

When $\varepsilon_2^{\mathrm{e}} = 0$ (25) reduces to (13). (25) is bounded between the following levels of hydrostatic stress

$$\xi_{b=0} = \frac{\sigma_c(1 + \nu) - (1 - 2\nu)(2 + k)\sigma^{\mathrm{e}}}{\sqrt{3}(\nu(1 + k) - 1)} \qquad \text{and} \qquad \xi_{b=1} = \frac{\sigma_c(1 + \nu) + (1 - 2\nu)\sigma^{\mathrm{e}}}{\sqrt{3}(k - \nu(1 + k))}. \tag{26}$$

EXAMINATION OF THE ORIENTATION OF σ_2

Before presenting the results for plane-strain M-C elasto-plasticity, we examine the validity of the assumption that the intermediate principal stress, σ_2, is the out-of-plane stress, σ_z. The first condition that should be considered is when the principal elastic strains in the in-plane directions are equal. In this case the stress in the out-of-plane direction (σ_{zz}) is either the major (σ_1) or the minor (σ_3) principal stress (depending on the sign of ε_2^e). The resultant stress state will be located on the compression ($b = 0$, for positive ε_2^e) or extension ($b = 1$, for negative ε_2^e) meridians with hydrostatic stresses less (15) or greater than (17) respectively.

A more interesting case is to consider an unstressed single material point, subjected to a stress increment of $\Delta\sigma_x = -200$kPa followed by a strain increment of $\Delta\varepsilon_y = -1\times10^{-3}$. In this illustrative example the material is modelled by a Young's Modulus of 100MPa, Poisson's ratio of 0.3, friction angle and dilation angle of $\pi/9$ and an apparent cohesion of 100kPa. The principal stress variation with (i) ε_y and (ii) normalised hydrostatic stress (ξ/c) is shown in Figure 2.

Application of $\Delta\sigma_x$ causes the stress to move from states 1 to 2 (see Figure 2) with $\sigma_z = \sigma_2$. From state 2, the stress in the x direction remains constant while a strain in the y direction is applied. At I the relative proportions of the principal stresses change such that σ_z is no longer the intermediate principal stress. Between I and III, σ_z is greater than both σ_x and σ_y. Along this path σ_y is initially the intermediate principal stress. Between II and III, σ_x is the intermediate principal stress. The ordering changes again at III where σ_z becomes the intermediate principal stress. Thereafter $\sigma_x > \sigma_z > \sigma_y$. The material yields at state 3, with the stresses remaining constant under continuous deformation. The direction of the principal stresses are shown schematically by the cuboids at the top of Figure 2, where the dashed grey and the solid unshaded cuboids show the original and final deformed shapes respectively.

This example shows that even for simple linear isotropic elasticity, the direction of the intermediate principal stress in plane-strain analyses is not necessarily directed out of the plane. However, in this example following yielding, σ_2 is the out-of-plane stress. In the examples which follow, the intermediate principal stresses always end up being the out-of-plane stresses.

FINITE-ELEMENT SIMULATIONS

9

Two-element simulation

A simple finite-element simulation using just two four-noded unit square fully-integrated quadri-

lateral elements is now considered (see Figure 3). Two upper surface nodes were subjected to vertical

displacements of $v = -0.01$m in 100 equal loadsteps. A Young's modulus of $E = 100$MPa and Pois-

son's ratio of $\nu = 0.3$ were used for the material's elastic properties. As in the previous example,

the associated flow M-C model had a friction angle of $\phi = \pi/9$ and a cohesion of 100kPa.

Figure 3 shows the ξ/c versus b paths for the integration points that underwent elasto-plastic

deformation during the analysis (that is, seven out of a total of eight integration points). The initial

states are identified by the white symbols and the states corresponding to a displacement of 10mm

are shown by the grey shaded symbols. Upon commencing inelastic straining, the Gauss point ξ

versus b paths reach the analytical solution provided by (14), as shown by the thick light grey line

in Figure 3. Under increasing deformation the stress states continue to move along that locus.

In order to highlight the differences between the *true* M-C yield surface and M-C formulations

where local curvature is introduced near the compression and extensions meridians, this simple two-

element simulation was analysed using the C2 continuous M-C surface of Abbo et al. (2011). Before

presenting the numerical results, the following disadvantages associated with rounding corners are

noted:

1. Implicit stress integration (for example, backward-Euler) of a smoothed M-C yield surface

will generally require multiple iterations to converge. Thus the rounded version of the M-C

is computationally more expensive in terms of both the material point stress integration and

the global solution scheme. There are also potential stability issues when returning near the

tensile apex on a smoothed yield surface. This is unlike the true M-C envelope, which will

always return in one step.

2. Rounding corners introduces errors into the stress integration procedure whereas the true

M-C envelope with sharp corners gives an exact stress integration solution (provided that the

corners are dealt with appropriately). Introducing rounding can prohibit the convergence

towards established analytical solutions (such as the Prandtl solution).

Introducing local curvature destroys the unique relationship between hydrostatic stress and the principal stress ratio, as shown in Figure 4. The smoothed M-C model of Abbo et al. (2011) requires a transition Lode angle, θ_t, where the M-C yield surface is smoothed for $|\theta| > \theta_t$. Here, θ_t was set to $\pi/9$ (20° degrees), corresponding to transition principal stress ratios, b_t, of 0.185 and 0.815. Once a stress state moves into the *rounded* region in the vicinity of the compression or extension meridians, the numerical ξ/c versus b paths disagree with the analytical solution (14).

As mentioned above, if appropriately constructed, an implicit stress integration routine for the true M-C envelope will always return in a single step. However, in order to achieve this, simple geometric rules must be formulated to identify the appropriate return position based on the trial stress state (see Clausen et al. (2006)). By operating in principal stress space, it is possible to identify which of the following return locations applies: (i) the planar surface or the intersection of two planes at (ii) the compression meridian or (iii) the extension meridian or (iv) the intersection of six planes at the tensile apex. This process circumvents the instability issues potentially associated with iterative approaches.

We now consider the cost of the numerical analysis. The model with local curvature in the yield surface required 250 global iterations whereas the *true* M-C yield surface only required 181. Also, the smoothed M-C model required multiple material point iterations to obtain convergence in the stress integration routine during each of these global iterations. The combination of these two factors resulted in a 255% increase in the overall run-time when using the smoothed M-C approximation.

Footing analysis

This section presents the numerical analysis of a one metre-wide rigid strip footing bearing onto a weightless soil using the M-C model. Due to symmetry, only one half of the 5-by-10 metre domain was discretised using 135 eight-noded quadrilateral elements with reduced four-point Gaussian quadrature (as shown to the right of Figure 5, where the lower inset figure shows the global discretisation and the upper figure shows the mesh refinement detail around the footing). This is the same mesh as adopted by de Souza Neto et al. (2008) and later used by Coombs et al. (2010) for the small strain analysis of frictional cone models. A Young's modulus of $E = 100$MPa and a

11

Poisson's ratio of $\nu = 0.3$ were used for the material's elastic properties. The M-C model again had a friction angle of $\phi = \pi/9$ and a cohesion of 100kPa. The analysis was performed using both associated ($\phi_g = \pi/9$) and non-associated ($\phi_g = \pi/18$) plastic flow rules. The rigid strip footing was subject to a uniform vertical displacement of 100mm in 100 equal loadsteps. The normalised pressure versus displacement response is shown in Figure 5.

The theoretical limit pressure for the M-C model, as given by the Prandtl (and Reissner) solution (see Yu (2006), amongst others for details) is

$$ p = c\Big(\tan^2\big(\pi/4 + \phi/2\big) \exp^{\pi\tan(\phi)} -1\Big) \cot(\phi). \tag{27} $$

This equation gives the limit pressure for a rigid footing bearing onto a weightless soil for the case of zero surface surcharge. For a friction angle of $\phi = \pi/9$, the normalised theoretical limit pressure is $(p/c) = 14.84$. Both the associated and non-associated flow simulations agree rather well with this theoretical limit load, having errors of just 0.46% and 0.74% respectively.

Figure 6 (i) shows the principal stress ratio versus normalised hydrostatic stress for the non-associated finite-element simulation at the end of the analysis (circular discrete points), the path taken to reach that state (fine grey lines) and the analytical ξ versus b solution (thick solid black line). Two Gauss point stress paths have been identified by fine black lines, starting at the grey squares (G and H) and finishing at the white circular symbols on the analytical solution locus. The final stress states and the elasto-plastic stress paths agree with the analytical solution, verifying the unique relationship between ξ and b provided by (14).

To highlight the special nature of the M-C constitutive formulation, the elasto-plastic ξ versus b points (at the end of the finite-element analysis) for a isotropic linear elastic-perfectly plastic Drucker-Prager model (Drucker and Prager, 1952) (referred to here simply as the D-P model) have been plotted on Figure 6 (ii). The non-associated flow D-P model used here had the same elastic properties as the M-C model. The conical D-P model has a circular deviatoric section with the yield surface centred on the hydrostatic axis. This yield envelope provides a simplified smooth approximation to the M-C yield criterion. In this analysis the D-P cone was chosen to coincide

12

with the M-C surface on the compression meridian. The square symbols in Figure 6 (ii) show that, unlike the M-C model, there is no unique ξ versus b plane-strain relationship for the D-P model.

The major difference between the M-C and the D-P models is that, for the D-P model, the yield surface

$$f = \rho + \alpha(\xi - \xi_c) = 0 \qquad (28)$$

has a dependence on the intermediate principal stress and thus the associated direction of plastic flow contains a component in the intermediate principal strain direction. The combination of these two features means that it is not possible to write a unique plane-strain relationship between the hydrostatic stress and the principal stress ratio for the D-P model. In (28), α is the opening angle of the D-P cone, here set to $\alpha = \tan(\phi)$, $\rho = \sqrt{2J_2}$ is a scalar measure of the deviatoric stress and $\xi_c = \sqrt{3}c\cot(\phi)$ identifies where the yield surface intersects the hydrostatic axis.

Finite deformation cylindrical cavity expansion

In this section we present an analysis of the expansion of a cylindrical soil cavity under internal pressure. Although this can be analysed as a one-dimensional axi-symmetric problem, here we use the two-dimensional plane-strain finite deformation finite-element code to make comparisons with an analytical solution and to provide further verification of the ξ-b relationship. Only a 3° segment of the structure (with internal radius of 1m and fixed outer boundary of radius 2km) was discretised using 50 four-noded plane-strain quadrilateral elements. The size of the elements was progressively increased by a factor 1.12 from the inner to the outer surface. A Young's modulus of $E = 100\text{MPa}$ and a Poisson's ratio of $\nu = 0.2$ were used for the material's elastic properties. The associated flow M-C model had a friction angle of $\phi = \pi/6$ and a cohesion of 100kPa. The internal radius was expanded to 5m using 80 equal displacement increments.

Due to this large change in internal radius, the effects of geometric non-linearity cannot be ignored. The M-C model described in this paper was implemented within a Lagrangian finite deformation finite-element code. The use of a logarithmic strain-Kirchhoff stress formulation, combined with an exponential map of the plastic flow, allows the incorporation of existing small strain constitutive algorithms without modifying their stress integration routine. This method is one of the

13

most successful and straight-forward ways of accounting for the additional geometric complexities inherent in finite deformation analyses when implementing large strain elasto-plasticity (Kim et al., 2009). The Kirchhoff stress, $[\tau]$ is defined as

$$[\tau] = J[\sigma], \tag{29}$$

where $[\sigma]$ is the Cauchy stress and J is the determinant of the deformation gradient. This volume ratio, J, is a measure of the change in volume between the current (deformed) configuration and the original reference state. See Coombs and Crouch (2011) and the references contained within for further information on the finite deformation finite-element formulation.

Figure 7 shows the normalised internal pressure (p/c) versus expansion ratio (a/a_0) response from the M-C finite deformation finite-element simulation (solid line), where a_0 and a are the original and current internal radii respectively. The numerical results display good agreement with the analytical solution (discrete points) provided by Yu and Houlsby (1991).

The unique ξ versus b relationship still holds for finite deformation analysis provided that the Cauchy hydrostatic stress in (13) and (14) is replaced by the equivalent Kirchhoff stress measure, namely

$$\xi_\tau = \mathrm{tr}\big([\tau]\big)/\sqrt{3}. \tag{30}$$

This is demonstrated in Figure 8, where the numerical elasto-plastic normalised Kirchhoff hydrostatic stress versus principal stress ratio points, at the end of the analysis, have been plotted alongside the analytical relationship (solid line). Note that additional stress states exist on the compression meridian where $\xi_\tau/c < -20$MPa. However, for clarity the abscissa has been limited to $\xi_\tau/c \in [-20, 5]$MPa. All of the finite-element Gauss points lie on the line described by the rational relationship (13).

Ewing and Griffiths (1971) investigated elasto-plastic stress concentrations around a notch for an isotropic elastic-perfectly plastic Tresca constitutive model. Their study was based on the plane-strain numerical analysis of Griffiths and Owen (1971). They found that the maximum stress was "attained inside the plastic zone surrounding the notch, not at its edge" (Ewing and Griffiths,

1971). This was due to plastic strains, comparable to the in-plane strains, being induced in the out-of-plane direction at material points where the stress state was located on the compression or extension meridians. Prompted by these findings, Figure 9 presents the normalised pressure versus expansion response of the cylindrical cavity following loading to an internal pressure of approximately 3MPa (corresponding to a expansion of $a/a_0 = 2$) and then unloading. The load-controlled numerical analysis was conducted using 100 steps in both the loading and unloading phases. The same material parameters as used in the previous cavity expansion simulation were used in this analysis. The elastic and elasto-plastic sections of the structural response are identified by the dashed grey and solid black lines respectively. The analysis starts at I and is loaded to III. The structure unloads elastically between III and IV until the reoccurrence of elasto-plastic deformation at IV which continues to V.

The normalised hydrostatic stress versus the principal stress ratio path of a Gauss point, located at an initial radial coordinate of 1.626m, is shown in Figure 9 (ii). Upon loading, the material point intersects with and moves along the locus described by (13). At II, the stress state reaches the compression meridian. On the compression meridian, the direction of plastic flow is no longer uniquely defined. However, the constitutive model's plastic strain increment (when subjected to a total strain increment) can be obtained using the method proposed by Koiter (1953). The non-uniqueness of the plastic strain direction leads to inelastic deformation in the out-of-plane direction when loading between II and III. That is, the assumption that $\varepsilon_2^{\mathrm{p}} = 0$, is invalidated and instead we have the condition $\varepsilon_2^{\mathrm{p}} = -\varepsilon_2^{\mathrm{e}}$. The effect of this non-zero out-of-plane elastic strain can be seen in Figure 9 (ii). Upon unloading, the stress state moves from III to IV, where it again encounters the yield surface. However, due to the non-zero $\varepsilon_2^{\mathrm{e}}$, the unloading elasto-plastic ξ/c versus b response (between IV and V) does not agree with the analytical solution (13). This solution is restricted to cases where stress states do not move on-to and subsequently away-from the corner or apex regions.

Figure 9 (ii) shows that the analytical solution when $\varepsilon_2^{\mathrm{e}} \neq 0$ agrees with the elasto-plastic stress path between IV and V. Along this path the Gauss point had an out-of-plane elastic strain of $\varepsilon_2^{\mathrm{e}} = -0.0032$. (25) allows an analytical relationship between ξ and b to be defined for material points that have non-zero elastic strain in the out-of-plane direction. It also supports the findings

15

of Ewing and Griffiths (1971) in that, for a given principal stress ratio, the hydrostatic stress (and hence $\{\sigma\}$) can change in magnitude for material points undergoing inelastic straining in the out-of-plane direction.

CONCLUSION

This paper has shown that when the out-of-plane stress is the intermediate principal stress there exists a unique relationship between hydrostatic pressure and the principal stress ratio (or equivalently the Lode angle) for isotropic M-C and Tresca linear elastic-perfectly plastic models in plane-strain analyses. This finding is verified using three numerical simulations, including the analysis of a rigid strip footing bearing onto a weightless soil and the finite deformation simulation of a cylindrical cavity expansion.

The single-valued function (13) and the extension to the case of $\varepsilon_2^{\mathrm{p}} \neq 0$ (25) provides new insight to the role of the intermediate principal stress in M-C and Tresca plane-strain analyses.

In this paper we have made use of established procedures for dealing with non-smooth yield surfaces (for example, see Clausen et al. (2006, 2007) which build on the work of Koiter (1953)). Some workers have introduced local curvature near the compression and extension meridians, when approximating the M-C model, in order to remove the corners (Abbo et al., 2011). We believe that this is quite unnecessary.

REFERENCES

Abbo, A., Lyamin, A., Sloan, S., and Hamble, J. (2011). "A C2 continuous approximation to the Mohr-Coulomb yield surface." *Int. J. Solids Struct.*, 48, 3001–3010.

Clausen, J., Damkilde, L., and Andersen, L. (2006). "Efficient return algorithms for associated plasticity with multiple yield planes." *Int. J. Numer. Meth. Engng*, 66, 1036–1059.

Clausen, J., Damkilde, L., and Andersen, L. (2007). "An efficient return algorithm for non-associated plasticity with linear yield criteria in principal stress space." *Comput. Struct.*, 85, 1795–1807.

16

Coombs, W. and Crouch, R. (2011). "Non-associated Reuleaux plasticity: analytical stress integration and consistent tangent for finite deformation mechanics." *Comput. Methods Appl. Mech. Engrg.*, 200, 1021–1037.

Coombs, W., Crouch, R., and Augarde, C. (2010). "Reuleaux plasticity: analytical backward Euler stress integration and consistent tangent." *Comput. Methods Appl. Mech. Engrg.*, 199, 1733–1743.

de Souza Neto, E., Perić, D., and Owen, D. (2008). *Computational methods for plasticity: Theory and applications.* John Wiley & Sons Ltd.

Drucker, D. and Prager, W. (1952). "Soil mechanics and plastic analysis or limit design." *Quart. Appl. Math*, 10, 157–164.

Ewing, D. and Griffiths, J. (1971). "The applicability of slip-line field theory to contained elastic-plastic flow around a notch." *J. Mech. Phys. Solids*, 19(6), 389–394.

Griffiths, J. and Owen, D. (1971). "An elastic-plastic stress analysis for a notched bar in plane strain bending." *J. Mech. Phys. Solids*, 19(6), 419–431.

Kim, D.-N., Montáns, F., and Bathe, K. (2009). "Insight into a model for large strain anisotropic elasto-plasticity." *Comput. Mech.*, 44(5), 651–668.

Koiter, W. (1953). "Stress-strain relations, uniqueness and variational theorems for elastic-plastic materials with a singular yield surface." *Quart. Appl. Math*, 11, 350–354.

Shield, R. (1955). "On Coulomb's law of failure in soils." *J. Mech. Phys. Solids*, 4, 10–16.

Yu, H.-S. (2006). *Plasticity and Geotechnics.* Springer.

Yu, H.-S. and Houlsby, G. (1991). "Finite cavity expansion in dilatant soils: loading analysis." *Géotechnique*, 41(2), 173–183.
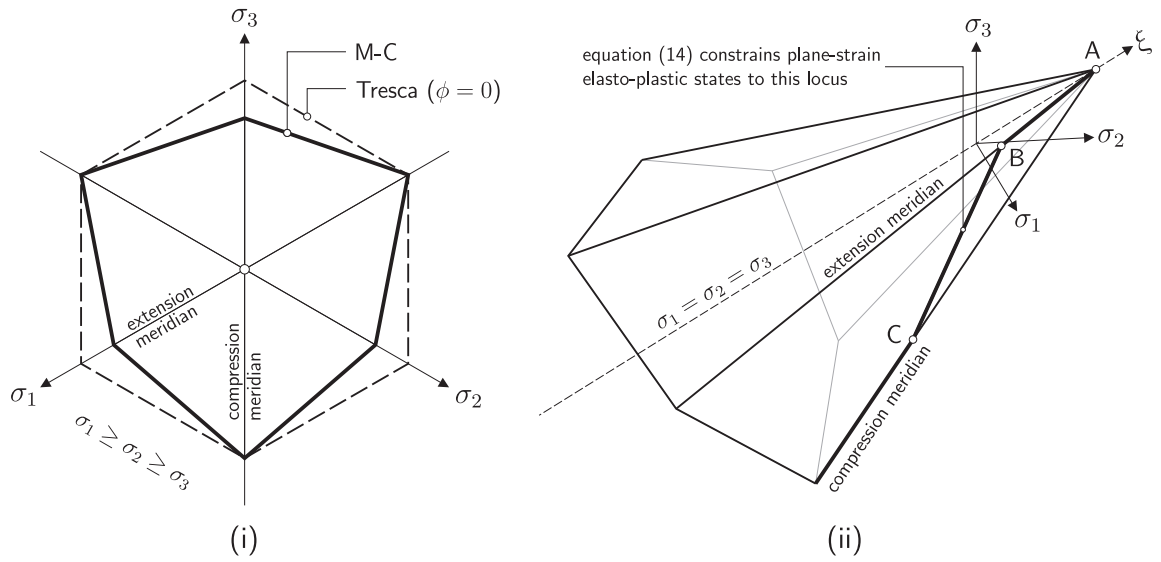
List of Figures

18

FIG. 1. Mohr-Coulomb yield surface: (i) **deviatoric section (including the Tresca yield criterion) and** (ii) **principal stress space including the plane-strain stress relationship (14).**
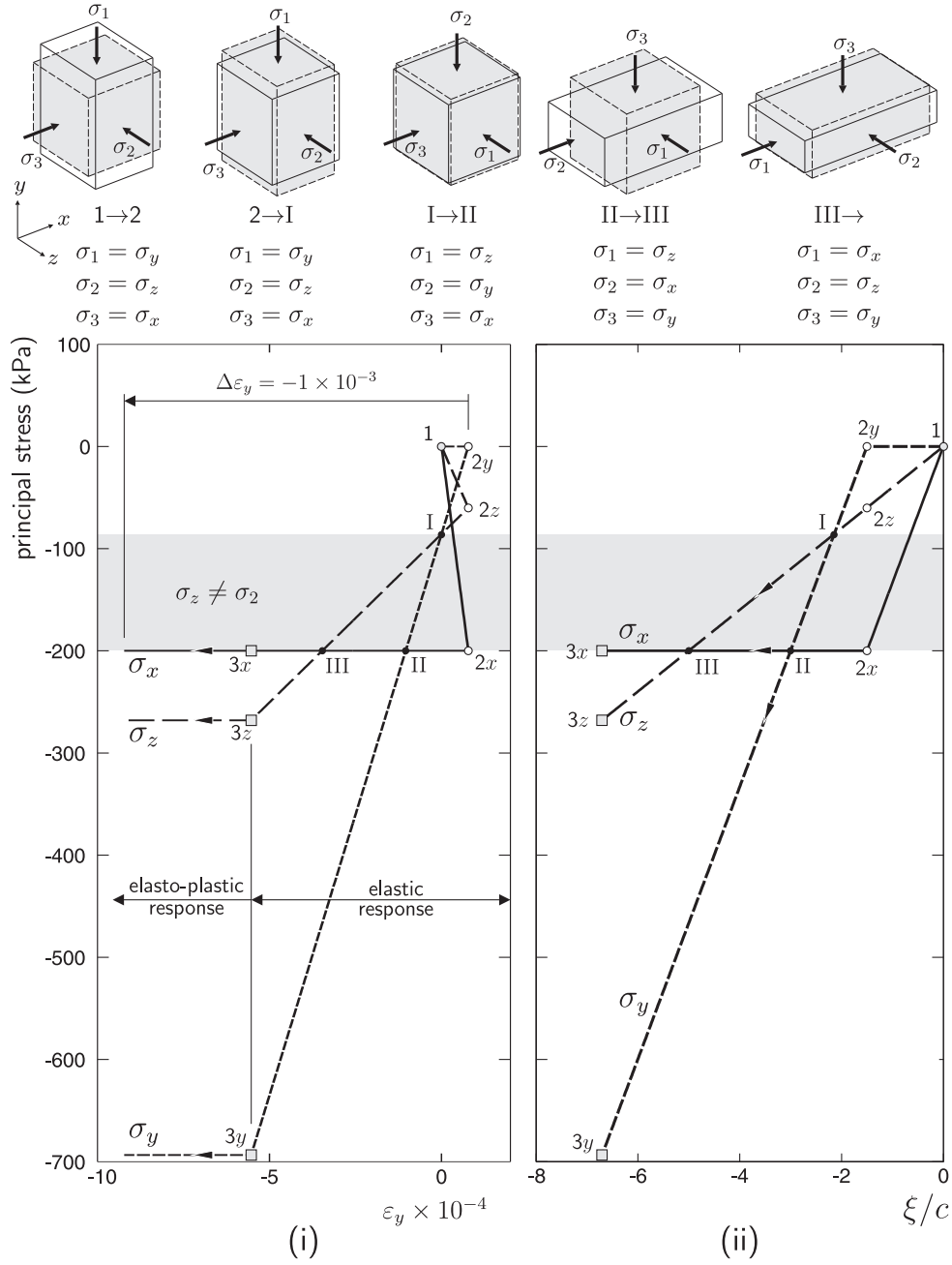
FIG. 2. Material point analysis: principal stresses against (i) **vertical strain** and (ii) **normalised hydrostatic stress,** ξ/c.
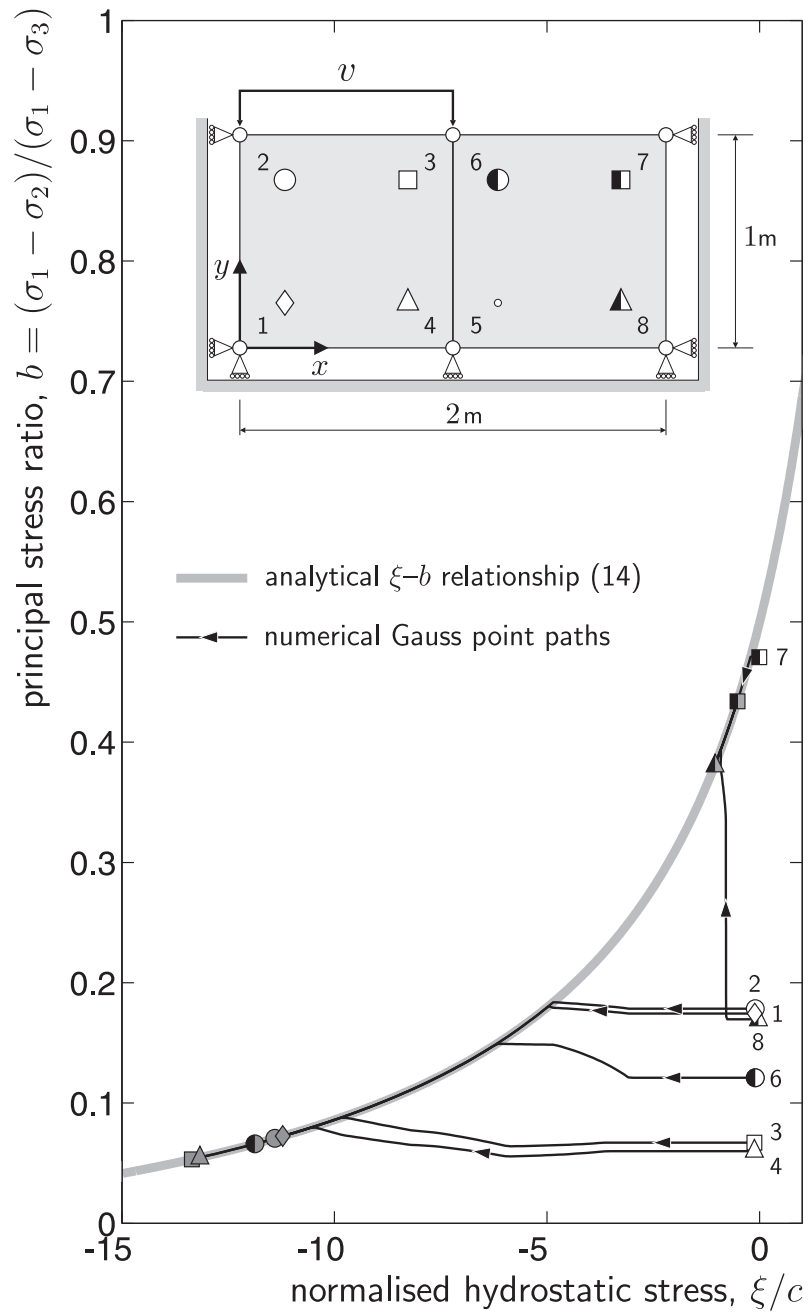
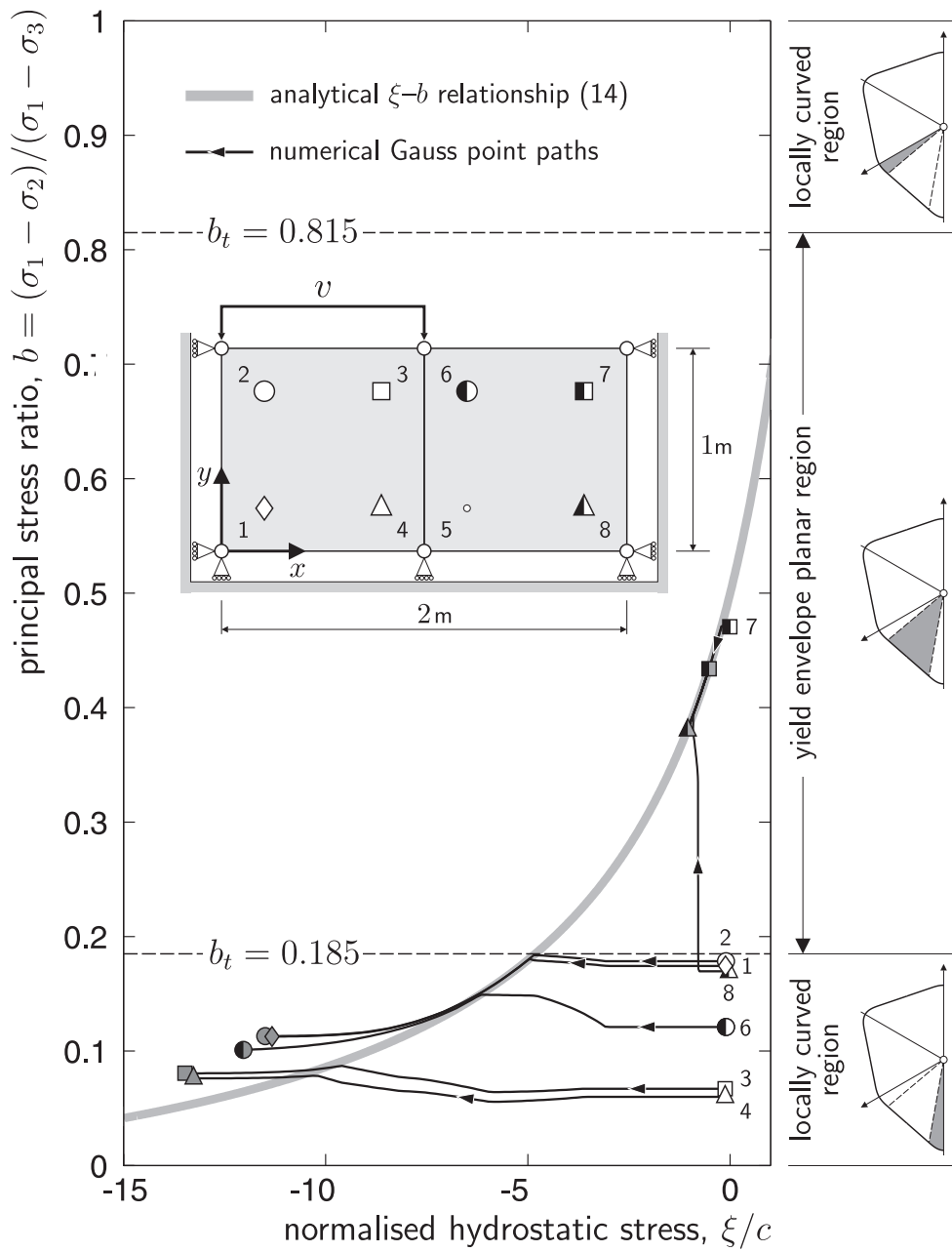**FIG. 3.** ξ/c versus b paths for the two-element simulation for $v \le 10$mm using the true M-C surface.

FIG. 4. ξ/c versus b paths for the two-element simulation for $v \le 10$**mm using the C2 continuous smoothed M-C surface of Abbo et al. (2011).**
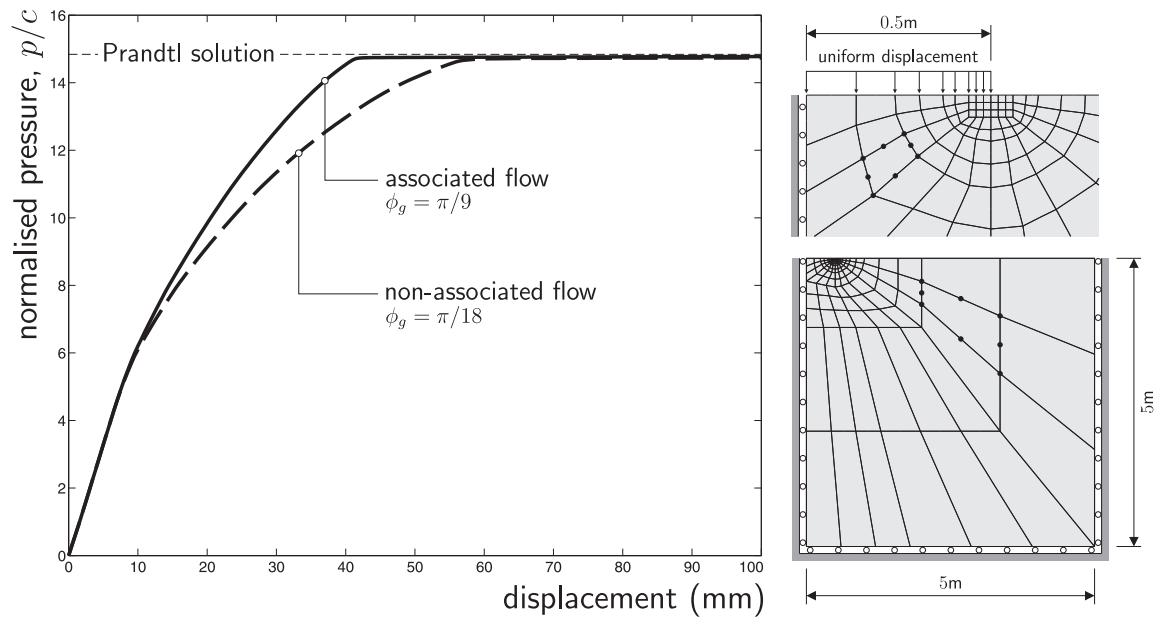
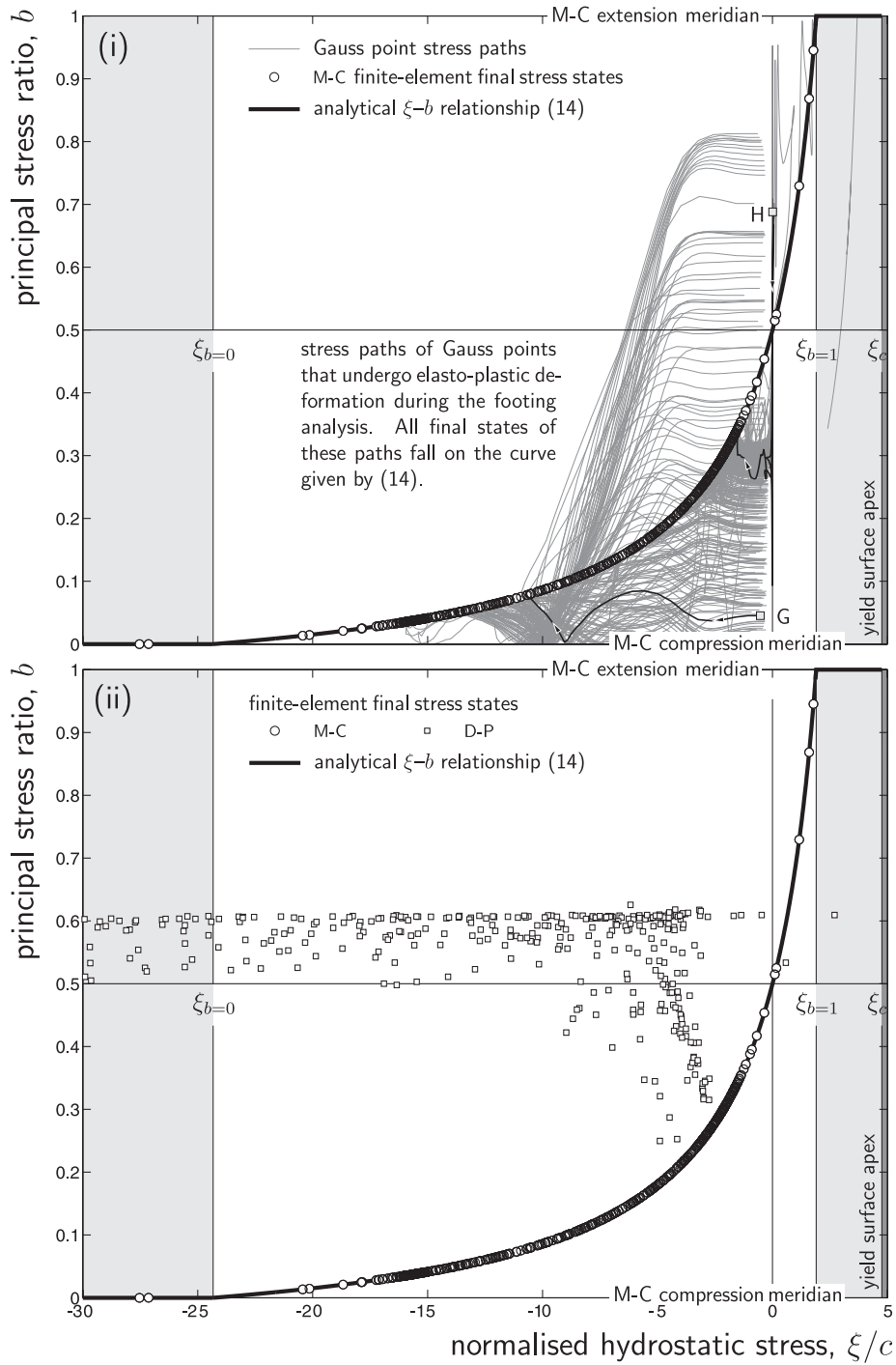FIG. 5. Rigid strip footing: p/c versus displacement response and finite-element discretisation.

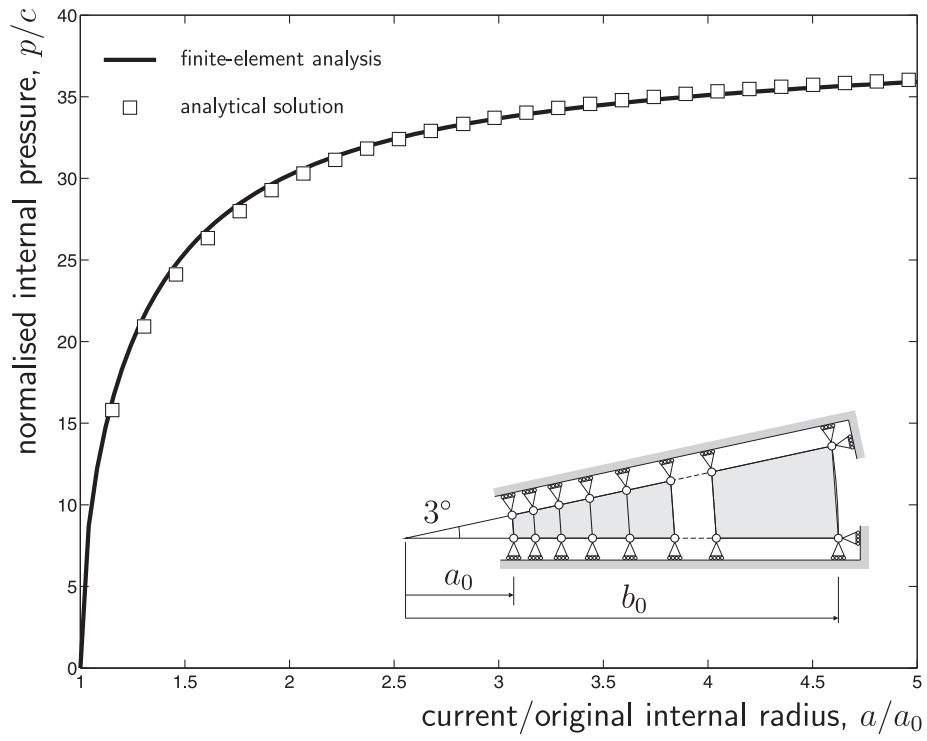FIG. 6.   Rigid strip footing: non-associated M-C ξ/c versus b response.
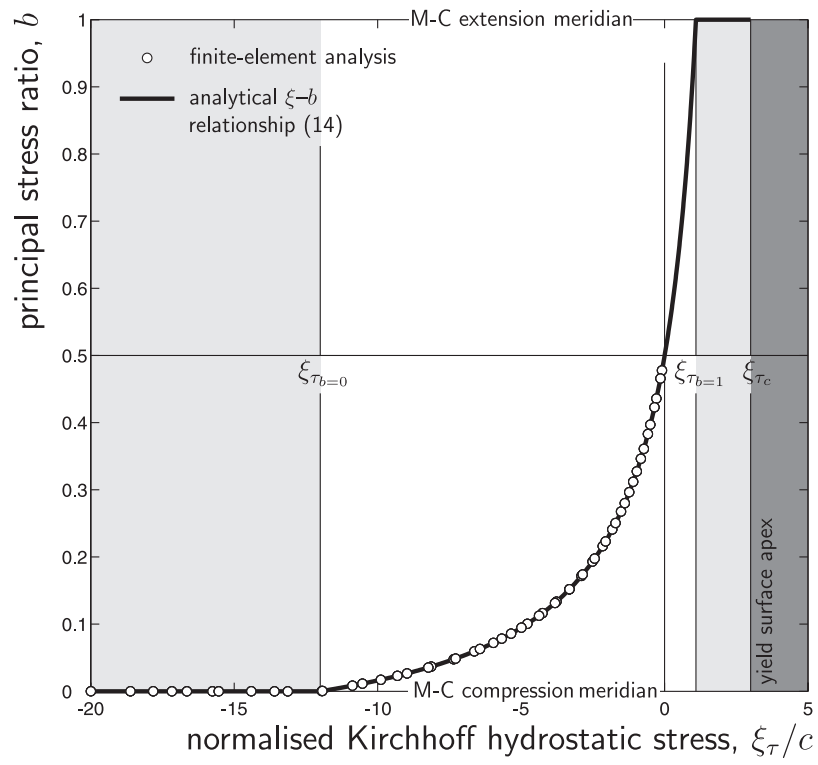
FIG. 7. **Cavity expansion:** p/c **versus** a/a_0.

FIG. 8. Cavity expansion: ξ_τ/c versus b response at the end of the analysis.
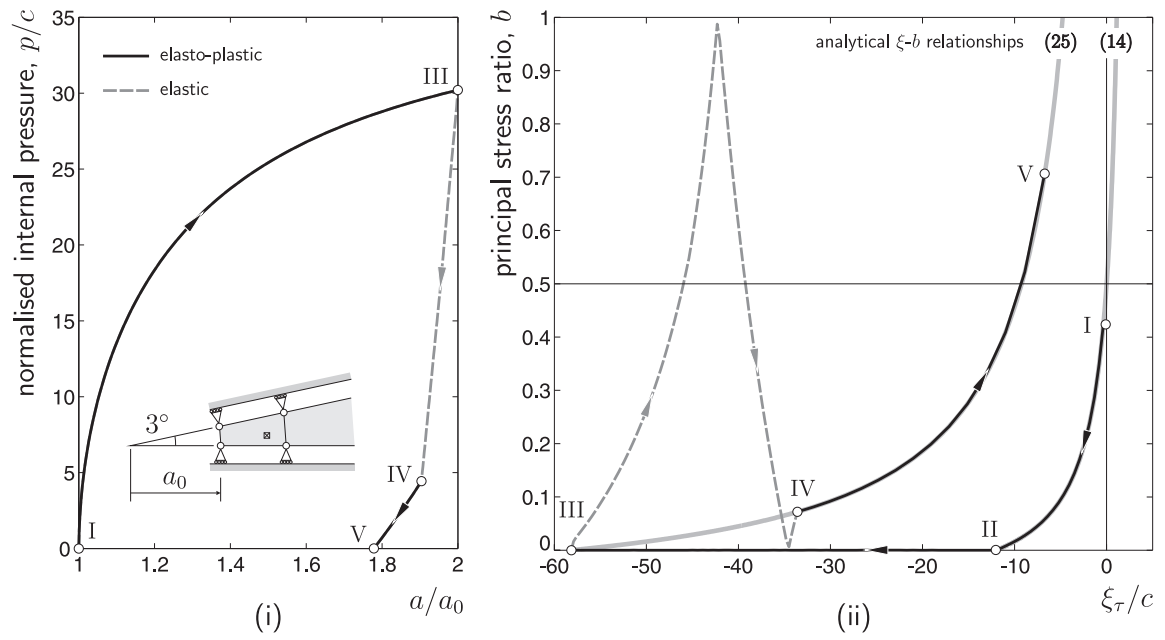
FIG. 9. Cavity expansion load-unload response: (i) p/c **versus** a/a_0 **and** (ii) ξ_τ/c **versus** b **path.**